Supplemental Materials for

Quasi-2D anomalous Hall Mott insulator of topologically engineered J_{eff} =1/2 electrons

Junyi Yang[1], Hidemaro Suwa[2], Derek Meyers[3,4], Han Zhang[1], Lukas Horak[5], Zhaosheng Wang[6], Gilberto Fabbris[7], Yongseong Choi[7], Jenia Karapetrova[7], Jong-Woo Kim[7], Daniel Haskel[7], Philip J. Ryan[7,8], M. P. M. Dean[3], Lin Hao[6,*], and Jian Liu[1,*]

[1]Department of Physics and Astronomy, University of Tennessee, Knoxville, Tennessee 37996, USA

[2]Department of Physics, University of Tokyo, Tokyo, Japan

[3]Department of Condensed Matter Physics and Materials Science, Brookhaven National Laboratory, Upton, New York 11973, USA

[4]Department of Physics, Oklahoma State University, Stillwater, OK 74078

[5]Department of Condensed Matter Physics, Charles University, Ke Karlovu 5, 12116 Prague, Czech Republic

[6]Anhui Key Laboratory of Condensed Matter Physics at Extreme Conditions, High Magnetic Field Laboratory, HFIPS, Chinese Academy of Sciences, Hefei, Anhui 230031, China

[7]Advanced Photon Source, Argonne National Laboratory, Argonne, Illinois 60439, USA

[8]School of Physical Sciences, Dublin City University, Dublin 9, Ireland

* To whom correspondence should be addressed. E-mail: haolin@hmfl.ac.cn, jianliu@utk.edu

This PDF file includes:
Figs. S1 to S10

1. Epitaxial relation analysis

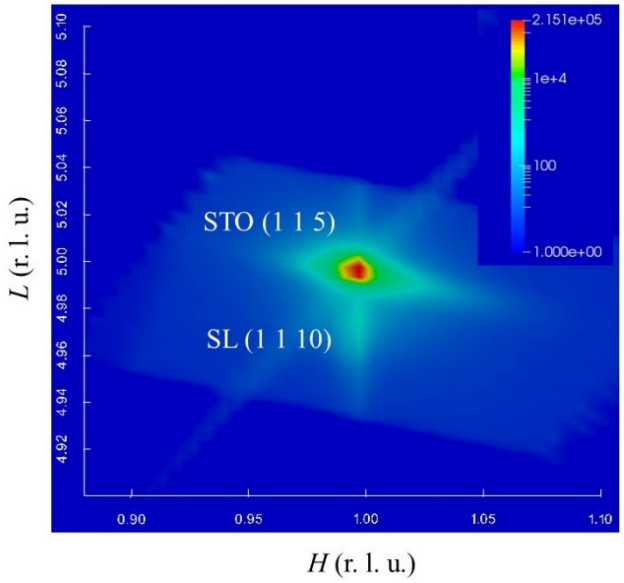

Fig. S1. Reciprocal space mapping around the (1 1 5) reflection of the $SrTiO_3$ substrate at room temperature. The reciprocal lattice is defined based on the substrate lattice.

Since the main Bragg reflections of the SL almost overlap with those of the substrate, here we checked the epitaxial relation via synchrotron-based reciprocal space mapping measurements. As shown in Fig. S1, the SL and the substrate have the same in-plane ***Q***-vectors, demonstrating that the SL is fully coherent with the underlying substrate.

2. Interface characterization

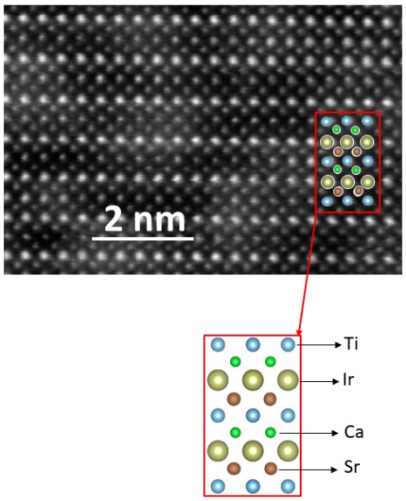

Fig. S2. Atomically resolved HAADF-STEM image of the SL along the surface normal direction. The schematic of crystal structure is also shown.

We performed STEM studies to directly visualize the interface of the SL. Figure S2 shows a representative image of the sample. One can see the obtained Z-contrast pattern is regular and displays a clear intensity modulation: the brightest spots correspond to the heaviest Ir ions and are well aligned in the (001) planes, with the interval equals to the *c*-axis lattice parameter of the SL unit cell. Meanwhile, weaker spots also located in the B-site between the Ir planes that correspond to the Ti ions. Their separation is half of the *c*-axis lattice parameter.

3. Octaheral rotation pattern characterization

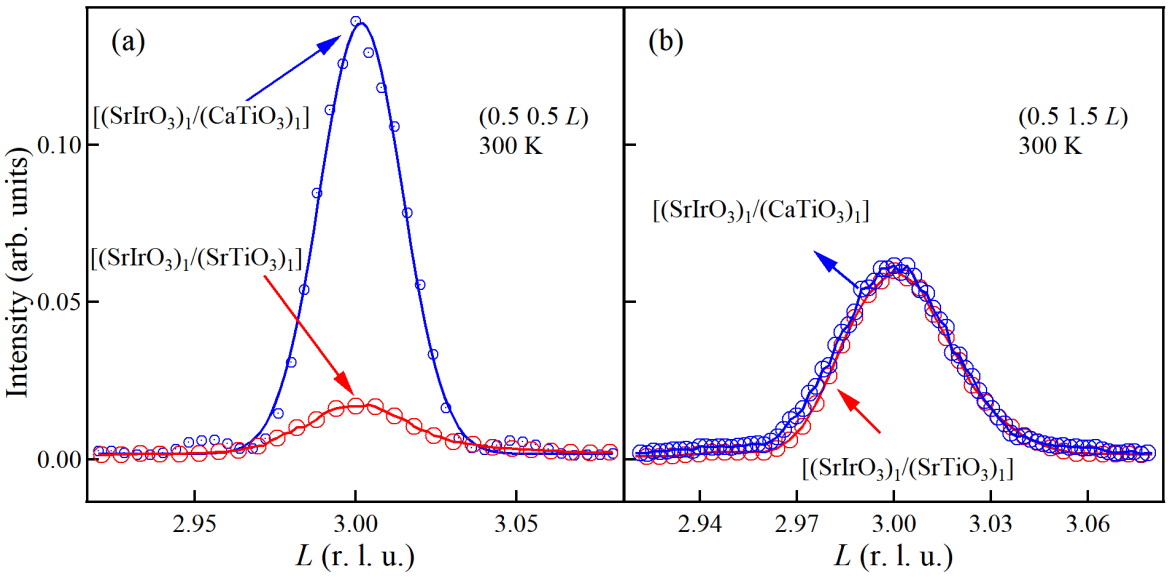

Fig. S3. *L*-scans covering the (0.5 0.5 3) (a) and (0.5 1.5 3) (b) Bragg peaks of two SLs. The reciprocal lattice is defined based on the unit cell of the SL.

We measured certain half-order structrual peaks to characterize the octahedral rotation pattern. According to the Glazer's seminar work [1], the octahedral tilt/rotation angle is proportional to the (0.5 0.5 3)/(0.5 1.5 3) peak intensity. Therefore, Fig. S3 demonstrates that $[(SrIrO_3)_1/(CaTiO_3)_1]$ has a much stronger octahedral tilt than the $[(SrIrO_3)_1/(SrTiO_3)_1]$ SL. The octahedral rotations, on the other hand, are quite similar in the two SLs.

4. Risitivity comparison between $[(SrIrO_3)_1/(CaTiO_3)_1]$ and $[(SrIrO_3)_1/(SrTiO_3)_1]$ SLs

As shown in Fig. S4, one can see that not only the room-temperature resistivity but also the resistivity increase when cooling to the base temperature are quite similar in the two SLs, indicating the similar electron correlation strangth in the two quasi-2D systems.

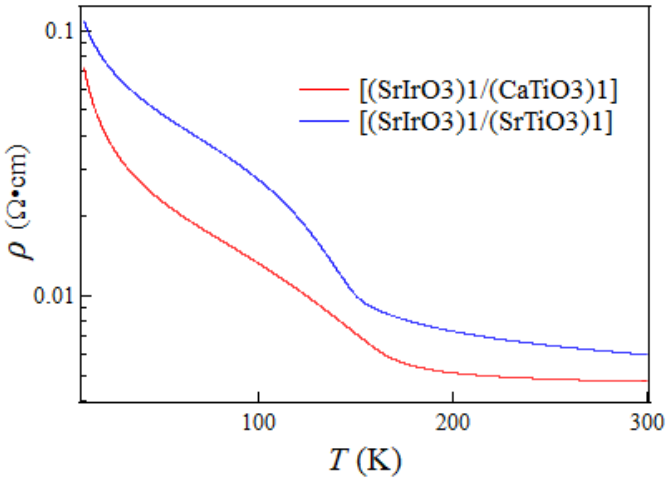

Fig. S4. Temperature dependent resistivity of $[(SrIrO_3)_1/(CaTiO_3)_1]$ (red) and $[(SrIrO_3)_1/(SrTiO_3)_1]$ (blue) SLs.

5. Hall measurements on $[(SrIrO_3)_1/(SrTiO_3)_1]$ SLs

We have measured Hall resistivity of the $[(SrIrO_3)_1/(SrTiO_3)_1]$ SLs grown on STO (T_N =150 K), LSAT (T_N =75 K) and NGO (T_N =55 K). Similar to the reported result in Ref. [2], we did not observe AHE effect for the $[(SrIrO_3)_1/(SrTiO_3)_1]$ SL grown on STO. Shown in Fig. S5 is representative Hall measurements on the $[(SrIrO_3)_1/(SrTiO_3)_1]$ SLs grown on LSAT and NGO below T_N, where no AHE is observed as well.

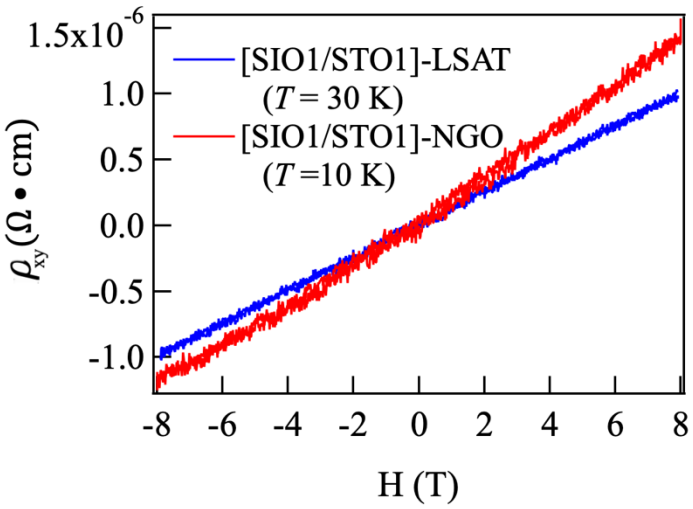

Fig. S5. Representative field dependent Hall resistivity of $[(SrIrO_3)_1/(SrTiO_3)_1]$ grown on LSAT at 30 K (blue) and NGO at 10 K (red).

6. Determination of σ_{xy}/σ_{xx} and S_H

We extracted Hall angle σ_{xy}/σ_{xx} from the remnant anomalous Hall conductivity and the resistivity measured under zero-field. In determining $S_H = \sigma_{xy}/M_s$, we used the saturated anomalous Hall conductivity. The AFM order parameter M_s is proportional to the square root of the integrated magnetic peak intensity. To match with the measured temperatures of the remnant anomalous Hall conductivity, the temperature dependent M_s was interpolated with a cubic spline function.

7. Berry curvature calculation

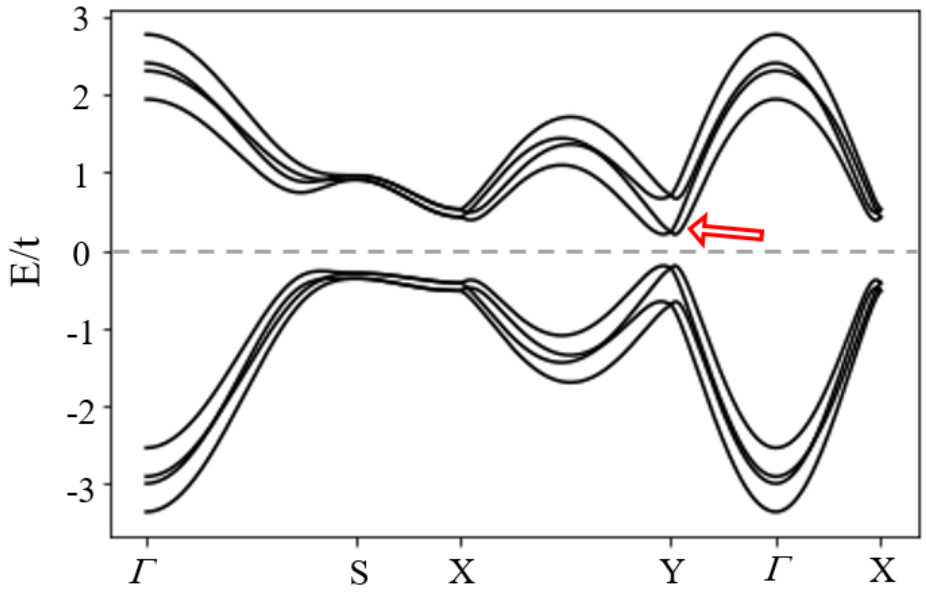

Fig. S6. Representative $U = 0$ band structure for the quasi-2D structure with an AFM order. The Fermi level is denoted by a dashed line. A valley-like feature is indicated by an arrow.

The dispersion in Fig.1d was calculated with the reported tight-binding model [3] that accounts for not only nearest neigohbor hopping but also the next-nearest neighbor hopping of J_{eff}=1/2 electrons under both rotation and tilt. The emergence of the AHE can be captured at the mean-field level by the Berry curvature near the valleys that originate from lifting the Dirac cone degeneracy by the AFM order, as shown in Fig. S6. The time-reversal degeneracy at other *k*-points is also lifted. We verified this by calculating the momentum-integrated Berry curvature of the bands in Fig.1d with the AFM moments perpendicular to the glide plane. To be consistent with the insulating behavior, we tuned the effective exchange field from the AFM order to obtain a band gap > 0.1 eV given that the typical size of the hopping parameter t is around 0.3 eV [3].

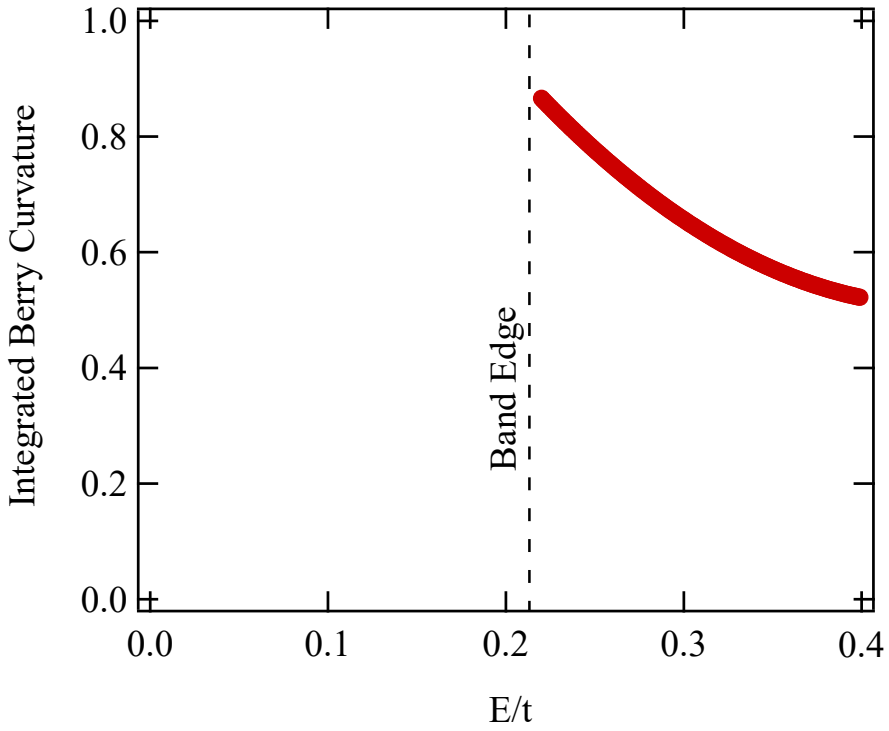

Fig. S7. Momentum-integrated Berry curvature as a function of energy near the conduction band edge from Fig. S6.

Since the carriers are thermally excited, we focus on the Berry curvature near the band edges, i.e., the valleys. Figure S7 plots the momentum-integrated Berry curvature as a function of energy for the conduction band. One can see a finite Berry curvature indeed emerges around 0.2t (0.06 eV) above the center of the charge gap, which is essentially the valley of the conduction band. The Berry curvature decreases as energy increases. The behavior near the valley of the valence band is same but with an opposite sign. Since the signs of the carriers (electron and hole) are also opposite, these opposite Berry curvatures constructively add up together and give rise to AHE. One should note that while the mean-field calculation qualitatively predicts the existence of Berry curvature, it is not expected to be able to quantitatively describe the AHE at finite temperature, particularly near the magnetic transition

temperature. This is because nonlinear fluctuations beyond the Gaussian fluctuations become significant near the transition temperature, not well incorporated in the existing approaches. Advanced analyses and sophisticated computational methods beyond mean-field-based approaches are required to account for the nontrivial temperature dependence of the Hall conductivity observed in our experiment and to provide a better understanding of the interplay of topology and electron correlation.

8. Characterization of Ir valence state and Ti Valence state

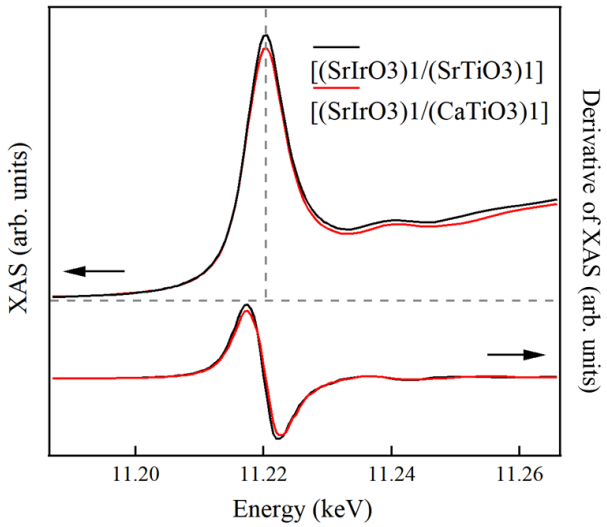

Fig. S8. Room-temperature energy dependence of XAS (left) and its derivative (right) of the $[(SrIrO_3)_1/(CaTiO_3)_1]$ (red). Data of the reference $[(SrIrO_3)_1/(SrTiO_3)_1]$ SL is also shown for comparison (black).

We performed x-ray absorption (XAS) measurement across the Ir-L_3 edge to characterize the Ir valence state of the SL. The white line peak position conincides with that measured on the reference $[(SrIrO_3)_1/(SrTiO_3)_1]$ SL [4] during the same experiment, which confirms the +4 valence state of Ir in the $[(SrIrO_3)_1/(CaTiO_3)_1]$ SL.

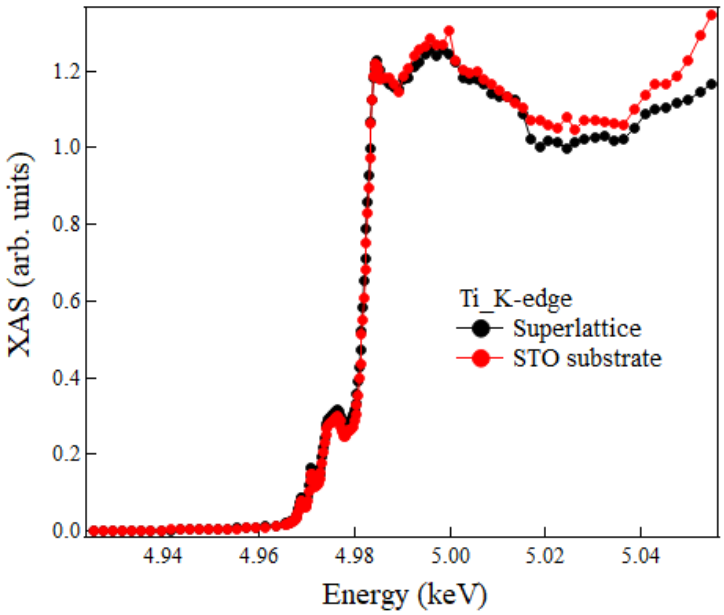

Fig. S9. X-ray absorption spectra around the Ti *K*-edge of the $[(SrIrO_3)_1/(CaTiO_3)_1]$ SL (black) and a $SrTiO_3$ substrate (red).

We also performed XAS measurement across the Ti-*K* edge to characterize the Ti valence state of the SL. As shown in Fig. S9, the SL displays essentially the same profile as the $SrTiO_3$ single crystal substrate, demonstrating that Ti is also at the nominal valence state of 4+.

9. Magnon gap analysis

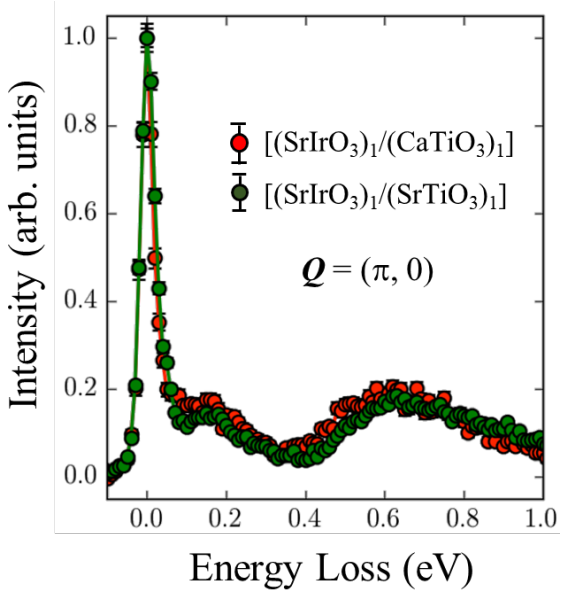

Fig. S10. RIXS spectra at $\boldsymbol{Q}$ = (π, 0) of $[(SrIrO_3)_1/(CaTiO_3)_1]$ (red) and $[(SrIrO_3)_1/(SrTiO_3)_1]$ (green) measured at 35 K.

RIXS spectra were collected at several $\boldsymbol{Q}$ points to map the dispersion of magnetic excitations. As another example, the spectra at $\boldsymbol{Q}$ = (π, 0) are shown in Fig. S10. The two SLs display a similar behavior at (π, 0), in sharp contrast to the large difference at (π, π). To extract the magnon excitation, we employed the same fitting procedure as demonstrated in a previous work[5], which gives a large magnon gap ~ 85±5 meV as mentioned in the main text. In the linear spin wave theory, the S=1/2 easy-axis XXZ model produces the magnon gap given by $\Delta_m = 2\sqrt{-2J \cdot \Gamma + \Gamma^2}$, where J is the nearest-neighbor exchange coupling, and $\Gamma < 0$ is the symmetric easy-axis anisotropy [6]. In the effective spin model [7], Γ is related to $D_\square$ via $|\Gamma| = \left|{D_\square}^2 / 32J\right|$. If we adopted the effective spin model and J = 53 meV of the $[(SrIrO_3)_1/(SrTiO_3)_1]$ SL [5], $\Delta_m = 85$ meV would imply $D_\square \sim 160$ meV in the $[(SrIrO_3)_1/(CaTiO_3)_1]$ SL, which means

the in-plane component of $\boldsymbol{D}_{ij}$ would be $D_{\square}/4 \sim 40$ meV. By assuming the same magnitude of the in-plane and out-of-plane components of $\boldsymbol{D}_{ij}$ reasonably expected from the magnetization measurement, we could obtain $\boldsymbol{D}_{ij} \sim 56$ meV. Via the second-order perturbation in the Hubbard model, it is known that $|\boldsymbol{D}_{ij}| = {8t^2}/{U} \cdot \tan\theta$ [8]. By taking $t \sim 0.1$ eV and $\theta = 10°$, we would estimate $U \sim 0.25$ eV and $U/t \sim 2.5$. Because the resultant U/t is far from the strong coupling limit, the above argument implies that the effective spin model is invalid for the $[(SrIrO_3)_1/(CaTiO_3)_1]$ SL.

10. Tempereature dependent RIXS measurement

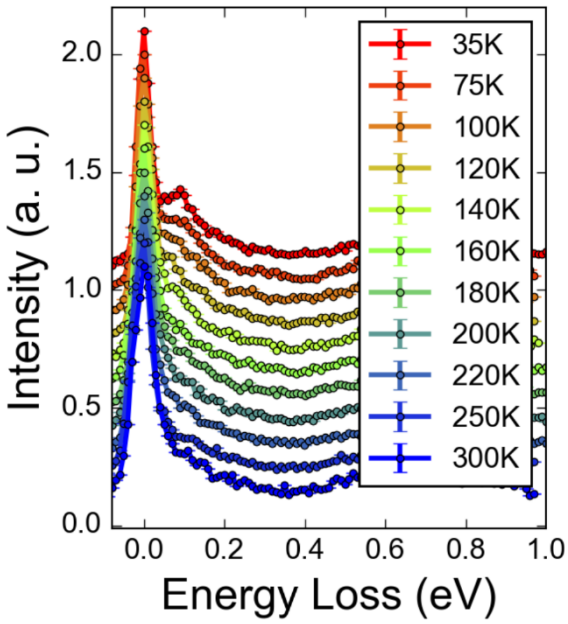

Fig. S11. Temperature dependent RIXS spectra at (π, π).

We measured temperature dependence of the RIXS spectra at (π, π), as shown in Fig. S11. As expected, the peak position remains the same, but the peak is broadening and eventually smeared out by thermal fluctuations.

References

[1] A.M. Glazer, *Simple ways of determining perovskite structures*, Acta Cryst. **A31**, 756-762 (1975).
[2] J. Matsuno, K. Ihara, S. Yamamura, H. Wadati, K. Ishii, V.V. Shankar, H.Y. Kee, and H. Takagi, *Engineering a Spin-Orbital Magnetic Insulator by Tailoring SLs*, Phys. Rev. Lett. **114**, 247209 (2015).
[3] Y. Chen, and H.-Y. Kee, *Topological phases in iridium oxide SLs: Quantized anomalous charge or valley Hall insulators*, Phys. Rev. B **90**, 195145 (2014).
[4] L. Hao, Z. Wang, J. Yang, D. Meyers, J. Sanchez, G. Fabbris, Y. Choi, J.-W. Kim, D. Haskel, P.J. Ryan, K. Barros, J.-H. Chu, M.P.M. Dean, C.D. Batista, and J. Liu, *Anomalous magnetoresistance due to longitudinal spin fluctuations in a Jeff = 1/2 Mott semiconductor*, Nat. Commun. **10**, 5301 (2019).
[5] D. Meyers, Y. Cao, G. Fabbris, N.J. Robinson, L. Hao, C. Frederick, N. Traynor, J. Yang, J. Lin, M.H. Upton, D. Casa, J.-W. Kim, T. Gog, E. Karapetrova, Y. Choi, D. Haskel, P.J. Ryan, L.

Horak, X. Liu, J. Liu, and M.P.M. Dean, *Magnetism in iridate heterostructures leveraged by structural distortions*, Sci. Rep. **9**, 4263 (2019).
[6] S. Kar, K. Wierschem, and P. Sengupta, *Magnons in a two-dimensional transverse-field XXZ model*, Phys. Rev. B **96**, 045126 (2017).
[7] L. Shekhtman, A. Aharony, and O. Entin-Wohlman, *Bond-dependent symmetric and antisymmetric superexchange interactions in La_2CuO_4*, Phys. Rev. B **47**, 174-182 (1993).
[8] L. Shekhtman, O. Entin-Wohlman, and A. Aharony, *Moriya's anisotropic superexchange interaction, frustration, and Dzyaloshinsky's weak ferromagnetism*, Phys. Rev. Lett. **69**, 836-839 (1992).